Mineralogical Magazine (2023), **87**, 943–954
doi:10.1180/mgm.2023.71

CAMBRIDGE UNIVERSITY PRESS

Article

Deynekoite, $Ca_9\square Fe^{3+}(PO_4)_7$ – a new mineral of the merrillite group from phosphide-bearing contact facies of paralava, Hatrurim Complex, Daba-Siwaqa, Jordan

Evgeny V. Galuskin[1], Marcin Stachowicz[2], Irina O. Galuskina[1], Krzysztof Woźniak[3], Yevgeny Vapnik[4], Mikhail N. Murashko[5] and Grzegorz Zieliński[6]

[1]Institute of Earth Sciences, Faculty of Natural Sciences, University of Silesia, Będzińska 60, 41-200 Sosnowiec, Poland; [2]Institute of Geochemistry, Mineralogy and Petrology, Faculty of Geology, University of Warsaw, Żwirki i Wigury 93, 02-089 Warszawa, Poland; [3]Department of Chemistry, University of Warsaw, Pasteura 1, 02-093 Warszawa, Poland; [4]Department of Geological and Environmental Sciences, Ben-Gurion University of the Negev, P.O.B. 653, Beer-Sheva 84105, Israel; [5]Institute of Earth Sciences, Saint-Petersburg State University, Universitetskaya Nab. 7/9, 199034 St. Petersburg, Russia; and [6]Polish Geological Institute – National Research Institute, Rakowiecka 4, 00-975 Warsaw, Poland

Abstract

Deynekoite, $Ca_9\square Fe^{3+}(PO_4)_7$ (*R*3*c*, $a = 10.3516(3)$Å, $c = 37.1599(17)$Å, $V = 3448.4(3)$Å^3 and $Z = 6$), a new mineral of the merrillite group was found in the contact facies of paralava of the Hatrurim Complex in the Daba-Siwaqa pyrometamorphic rock field, Jordan. The paralava, consisting of diopside, tridymite, anorthite, wollastonite and fluorapatite, is enriched in Fe-bearing phosphides and phosphates at the contact with the altered country rock. Cristobalite overgrowing tridymite has a fish-scales texture indicating that temperature of paralava could have reached 1500°C. Deynekoite with empirical formula $(Ca_{8.90}Na_{0.11}K_{0.02})_{\Sigma 9.03}(Fe^{3+}_{0.62}Mg_{0.30}Al_{0.05})_{\Sigma 0.97}P_{6.98}V^{5+}_{0.05}O_{27.70}(OH)_{0.30}$ forms transparent, light-yellow or light-brown grains up to 30–40 μm in size. Microhardness of deynekoite, VHN_{25} = 319(29) kg/mm^2, corresponds to Mohs hardness = 4.5. Its density was calculated as 3.09 g·cm^{-3} on the basis of its empirical composition and structural data. Deynekoite is uniaxial (−), its refractive indices are $\omega = 1.658(3)$, $\varepsilon = 1.652(3)$ ($\lambda = 589$ nm), and pleochroism is not observed. The formation of phosphides on the boundary of the paralava and country rock is connected with carbothermal reductive reactions and realised at temperatures above 1300°C. With decreasing temperature and increasing oxygen activity, phosphides are replaced by Fe^{2+}-bearing phosphates. Deynekoite, which contains Fe^{3+} (substituting for Fe^{2+}-phosphates) and a small amount of water, formed at temperatures of 600–800°C.

Keywords: merrillite; deynekoite; paralava; Hatrurim Complex; Jordan

(Received 25 July 2023; accepted 29 August 2023; Accepted Manuscript published online: 11 September 2023; Associate Editor: Daniel Atencio)

Introduction

Deynekoite, $Ca_9\square Fe^{3+}(PO_4)_7$ (*R*3*c*, $a = 10.3516(3)$ Å, $c = 37.1599(17)$ Å, $V = 3448.4(3)$ Å^3 and $Z = 6$), a new mineral isostructural with merrillite, was found in the phosphide-bearing contact facies of diopside–anorthite–tridymite paralava of the Hatrurim Complex in Jordan. According to the cerite supergroup classification, deynekoite belongs to the merrillite subgroup. Together, the merrillite subgroup and the whitlockite subgroup form the merrillite group (Table 1; Atencio and Azzi, 2020). The general formula of minerals of the merrillite group can be presented as follows: $(A1_3A2_3A3_3)_{\Sigma 9}XM(P1O_4)_3$ $(P2O_3\emptyset)_3(P3O3\emptyset)$, where A = Ca, Sr and Na; X = Na, Ca and vacancy (□); M = Mg, $Fe^{2+,3+}$ and Mn^{2+}; P = P; $\emptyset$ = O and OH. Deynekoite is the first mineral of the merrillite group whose composition includes Fe^{3+}; it has a synthetic analogue (Lazoryak *et al.*, 1996; Benarafaa *et al.*, 2000; Deyneko *et al.*, 2014).

Minerals of the merrillite group (merrillite, $Ca_9NaMg(PO_4)_7$, keplerite, $Ca_9(Ca_{0.5}\square_{0.5})Mg(PO_4)_7$, and the potentially new mineral $Ca_8Y\square Mg(PO_4)_7$, forming a solid solution) were found recently in hematite-bearing diopside paralava hosted by the rocks of the 'olive unit', in the Negev Desert, Hatrurim Basin, Israel (Galuskina *et al.*, 2016; Britvin *et al.*, 2021b).

Merrillite is one of the most common phosphates in meteorites of different types and forms a solid solution with ferromerrillite, $Ca_9NaFe^{2+}(PO_4)_7$, which is typical for Martian shergottites (Britvin *et al.*, 2016; Ward *et al.*, 2017). OH-bearing minerals of the merrillite group (whitlockite subgroup) occur only in terrestrial rocks (Frondel, 1943; Britvin *et al.*, 1991; Cooper *et al.*, 2013).

In this paper, we provide a description of a new mineral, deynekoite, and discuss common problems in the classification of the merrillite group. We also consider the mechanism and conditions of deynekoite formation in phosphide-bearing contact facies of paralava from Jordan. The mineral and its name (symbol Dnk) have been approved by the Commission on New Minerals,

Corresponding author: Evgeny V. Galuskin; Email: evgeny.galuskin@us.edu.pl
Cite this article: Galuskin E.V., Stachowicz M., Galuskina I.O., Woźniak K., Vapnik Y., Murashko M.N. and Zieliński G. (2023) Deynekoite, $Ca_9\square Fe^{3+}(PO_4)_7$ – a new mineral of the merrillite group from phosphide-bearing contact facies of paralava, Hatrurim Complex, Daba-Siwaqa, Jordan. *Mineralogical Magazine* **87**, 943–954. https://doi.org/10.1180/mgm.2023.71

Table 1. Minerals of the merrillite group.

	*A*1+*A*2+*A*3	*X*	*M*	($P1O_4$)	($P2O_3Ø$)	($P3O_3Ø$)	End-member/simplified IMA formula	Reference
Merrillite subgroup								
Merrillite	Ca_9	Na	Mg	$(PO_4)_3$	$(PO_4)_3$	(PO_4)	$Ca_9NaMg(PO_4)_7$	Wherry (1917)
Ferromerrillite	Ca_9	Na	Fe^{2+}	$(PO_4)_3$	$(PO_4)_3$	(PO_4)	$Ca_9NaFe^{2+}(PO_4)_7$	Britvin *et al.* (2016)
Keplerite	Ca_9	$Ca_{0.5}□_{0.5}$	Mg	$(PO_4)_3$	$(PO_4)_3$	(PO_4)	$Ca_9(Ca_{0.5}□_{0.5})Mg(PO_4)_7$	Britvin *et al.* (2021b)
Matyhite	Ca_9	$Ca_{0.5}□_{0.5}$	Fe^{2+}	$(PO_4)_3$	$(PO_4)_3$	(PO_4)	$Ca_9(Ca_{0.5}□_{0.5})Fe^{2+}(PO_4)_7$	Hwang *et al.* (2019)
Deynekoite	Ca_9	□	Fe^{3+}	$(PO_4)_3$	$(PO_4)_3$	(PO_4)	$Ca_9Fe^{3+}(PO_4)_7$	This study
Changesite-(Y)	Ca_8Y	□	Fe^{2+}	$(PO_4)_3$	$(PO_4)_3$	(PO_4)	$Ca_8Y□Fe^{2+}(PO_4)_7$	Li *et al.* (2022)
Whitlockite subgroup								
Whitlockite	Ca_9	□	Mg	$(PO_4)_3$	$(PO_4)_3$	(PO_3OH)	$Ca_9Mg(PO_4)_6(PO_3OH)$	Frondel (1943)
Strontiowhitlockite	Sr_9	□	Mg	$(PO_4)_3$	$(PO_4)_3$	(PO_3OH)	$Sr_9Mg(PO_4)_6(PO_3OH)$	Britvin *et al.* (1991)
Wopmayite	Ca_6Na_3	□	Mn^{2+}	$(PO_4)_3$	$(PO_3OH)_3$	(PO_3OH)	$Ca_6Na_3□Mn(PO_4)_3(PO_3OH)_4$	Cooper *et al.* (2013)
Hedegaardite*	Ca_7Na_2	Ca	Mg	$(PO_4)_3$	$(PO_4)_3$	(PO_3OH)	$(Ca,Na)_9(Ca,Na)Mg(PO_4)_6(PO_3OH)$	Witzke *et al.* (2015)

* Hedegaardite was approved by the CNMNC-IMA in 2015, however a paper describing the mineral has not been published yet, so the most probable cation distribution among different sites is shown.

Nomenclature and Classification (CNMNC) of the International Mineralogical Association (IMA), as IMA 2020-108 (Galuskin *et al.*, 2022b). The name deynekoite is given in honour of Dr Dina V. Deyneko (born 1988) for her valuable contribution to the investigation of synthetic analogues of merrillite-group minerals (Deyneko *et al.*, 2014). Type material was deposited in the mineralogical collection of the Fersman Mineralogical Museum, Leninskiy pr., 18/k. 2, 115162 Moscow, Russia, registration number: 5791/1.

Methods of investigation

The morphology and composition of deynekoite and associated minerals were studied using optical microscopy, scanning electron microscopes (Phenom XL and Quanta 250, Institute of Earth Sciences, Faculty of Natural Sciences, University of Silesia, Sosnowiec, Poland) and an electron microprobe analyser (Cameca SX100, Micro-Area Analysis Laboratory, Polish Geological Institute – National Research Institute, Warsaw, Poland). Chemical analyses were carried out in WDS-mode (wavelength-dispersive X-ray spectroscopy, settings: 15 keV, 20 nA and ~1 μm beam diameter) using the following lines and standards: Na*K*α – NaCl; Ca*K*α and Mg*K*α – diopside; Al*K*α and K*K*α – orthoclase; Fe*K*α – Fe_2O_3; and V*K*α – V. Other chemical elements were below the detection limit.

The Raman spectra of deynekoite were recorded on a WITec alpha 300R Confocal Raman Microscope (Department of Earth Science, University of Silesia, Poland) equipped with an air-cooled solid laser (532 nm) and a CCD camera operating at −61°C. An air Zeiss LD EC Epiplan-Neofluan DIC-100/0.75NA objective was used. Raman scattered light was focused onto a multi-mode fibre and monochromator with a 600 mm^{-1} grating. The power of the laser at the sample position was ~30 mW, and 15–20 scans with an integration time of 3–5 s were collected and averaged. The resolution was 3 cm^{-1}. The spectrometer monochromator was calibrated using the Raman scattering line of a silicon plate (520.7 cm^{-1}).

Single-crystal X-ray studies were carried out with a four-circle diffractometer SuperNova with Ag*K*α radiation (λ = 0.56087 Å) (University of Warsaw Biological and Chemical Research Centre), equipped with an Eos CCD detector (Agilent). The detector-to-crystal distance was 63.2 mm. Ag*K*α radiation was used at 65 kV and 0.6 mA. Crystals were attached to a non-diffracting Mitegen micromount support. A frame-width of 1° in ω scans and a frame time of 410 s were used for data collection. Information relevant to the data collection is summarised in Table 2. Reflection intensities were corrected for Lorentz, polarisation and absorption effects and converted to structure factors using *CrysAlisPro 1.171.40.53* (Rigaku Oxford Diffraction, 2019) software.

Geological setting

Deynekoite was found in a small phosphorite prospecting quarry (31°22'01''N, 36°11'10''E) in the Daba-Siwaqa pyrometamorphic

Table 2. Crystal data and structure refinement details for deynekoite.

Crystal data	
Chemical formula	$Ca_9H_{0.27}Fe_{0.57}Mg_{0.42}Na_{0.09}O_{28}P_7$
M_r	1067.88
Crystal system, space group	Trigonal, *R*3*c* (161)
Temperature (K)	296
a, *c* (Å)	10.3516 (3), 37.1599 (17)
V (Å^3)	3448.4 (3)
Z	6
Data collection	
Diffractometer	Rigaku - Oxford Diffraction four circle diffractometer with a mirror monochromator, SuperNova, Single source, Ag, Eos detector
Radiation type	Ag *K*α, λ = 0.56087 Å
μ (mm^{-1})	1.53
Crystal size (mm)	0.03 × 0.03 × 0.02
Absorption correction	Multi-scan *CrysAlis PRO* 1.171.40.53 (Rigaku Oxford Diffraction, 2019) Empirical absorption correction using spherical harmonics, implemented in *SCALE3 ABSPACK* scaling algorithm.
T_{min}, T_{max}	0.989, 1.000
No. of measured, independent and observed [$I > 2\Sigma(I)$] reflections	6400, 1915, 1682
R_{int}	0.044
$(\sin\theta/\lambda)_{max}$ (Å^{-1})	0.704
Refinement	
$R[F^2 > 2\Sigma(F^2)]$, $wR(F^2)$*, GooF	0.041, 0.051, 1.04
No. of reflections	1915
No. of parameters	149
No. of restraints	4
H-atom treatment	Only H-atom coordinates refined
$\Delta\rho_{max}$, $\Delta\rho_{min}$ (*e* Å^{-3})	0.62, −0.58
Absolute structure	Refined as an inversion twin.
Absolute structure parameter	0.56 (10)

*$w = 1/[\Sigma^2(F_o^2) + (0.0236P)^2]$, where *P* is $[2Fc^2 + Fo^2)]/3$

https://doi.org/10.1180/mgm.2023.71 Published online by Cambridge University Press

rock field, Hatrurim Complex, Jordan (Novikov *et al.*, 2013; Khoury *et al.*, 2016). The Hatrurim Complex is distributed along the Dead Sea rift as a series of outcrops of pyrometamorphic rocks in the territories of Israel, Palestine and Jordan (Bentor, 1960; Gross, 1977, 1984; Vapnik *et al.*, 2007; Novikov *et al.*, 2013). The Hatrurim Complex is characterised by a wide diversity of rocks. Spurrite marble, larnite pseudoconglomerate and gehlenite hornfels dominate; however, there are also exotic rock types containing such rock-forming minerals as ye'elimite, $Ca_4Al_6(SO_4)O_{12}$; fluormayenite, $Ca_{12}Al_{14}O_{32}F_2$; nabimusaite, $KCa_{12}(SiO_4)_4(SO_4)_2O_2F$; ariegilatite, $BaCa_{12}(SiO_4)_4(PO_4)_2F_2O$; jasmundite, $Ca_{11}(SiO_4)_4O_2S$; ternesite, $Ca_5(SiO_4)_2(SO_4)$; levantite, $KCa_3Al_2(SiO_4)(Si_2O_7)(PO_4)$; silicocarnotite, $Ca_5(PO_4)_2(SiO_4)$; oldhamite, CaS_2; khesinite, $Ca_4(Mg_2Fe^{3+}_{10})O_4(Fe^{3+}_{20}Si_2)O_{36}$; and others (Galuskina *et al.*, 2017a; Galuskin *et al.*, 2016, 2019, 2021, 2023a). In the Hatrurim Complex, molten rocks that are diverse in composition form veins, lenses and oval bodies of paralavas and slag-like rocks from a few centimetres to tens of metres in size (Galuskin *et al.*, 2015; Galuskina *et al.*, 2017a, 2017b, 2017c; Krzątała *et al.*, 2020; Krüger *et al.*, 2021; Murashko *et al.*, 2022). It is the paralavas, which feature relatively coarser-grained rocks compared to other types of pyrometamorphic rocks, that are associated with the discovery of a significant number of new minerals. One example is the diopside–anorthite–tridymite paralava which forms a body ~30 m in diameter in pyrometamorphically altered carbonate rock of the Muwaqqar Chalk–Marl Formation, Daba-Siwaqa, Jordan. Deynekoite and a series of new minerals presented by both reduced (phosphides) and oxidised (phosphates containing Fe^{3+}) phases were discovered at the contact facies of this paralava. The phosphides discovered were transjordanite, Ni_2P; zuktamrurite, FeP_2; murashkoite, FeP; orishchinite, Ni_2P; and nickolayite, FeMoP. The phosphates were crocobelonite, $CaFe^{3+}(PO_4)O$; moabite, $NiFe^{3+}(PO_4)O$; yakubovichite, $CaNi_2Fe^{3+}(PO_4)_3$; and nazarchukite, $Ca_2NiFe^{3+}_2(PO_4)_4$ (Britvin *et al.*, 2019a, 2019b, 2020, 2021a, 2021b, 2022a, 2022b, 2023a, 2023b; Murashko *et al.*, 2022).

The genesis of the Hatrurim Complex rocks remains an unsolved problem. The early 'classic hypothesis' stated that pyrometamorphic rocks formed as a result of the spontaneous combustion of bitumen, which was contained in a sedimentary protolith (Kolodny and Gross, 1974; Matthews and Gross, 1980; Geller *et al.*, 2012). The relatively recent 'mud volcano' hypothesis suggests that deep anomalous pressure in the sedimentary sequence caused by the tectonic activity of the Dead Sea Rift affected the destruction of hydrocarbon collectors, inducing subsequent methane combustion in the vicinity of the surface (Sokol *et al.*, 2010; Novikov *et al.*, 2013). Our investigation shows that the reactions of combustion by-products (hot gases, fluids and melts) with the pyrometamorphic phases formed earlier sharply increased the mineral diversity of the rocks (Galuskin *et al.*, 2016, 2019).

Deynekoite occurrence

The paralava studied presents a dense, fine-grained rock in which porous, pumice-like fragments are distributed in an undulating pattern (Fig. 1a). It consists of diopside with hedenbergite rims, wollastonite, anorthite, tridymite, fluorapatite and a small amount of glass (Fig. 1b). The presence of cristobalite with typical fissures showing a fish-scale texture indicates that tetragonal cristobalite is a product of phase transition and the primary crystallisation of the mineral was as a high-temperature cubic phase, growing on tridymite (Fig. 1c). In thin apophyses of paralava into the country rock, pseudomorphs of fluorapatite after fish bones were detected (Fig. 1d). Accessory minerals of the paralava include spinel of the magnesiochromite–chromite–magnetite–trevorite series, titanite and pyrrhotite.

Minerals of the merrillite group forming a solid solution of merrillite–keplerite–deynekoite–whitlockite occur in a thin dark zone on the boundary of paralava and altered country rock (Fig. 2a). A contact facies of paralava has been strongly altered by low-temperature processes. Here, prismatic diopside crystals with composition close to ideal and up to 1 cm in size are embedded in a low-temperature mineral matrix containing primarily calcite and zeolites, among which gismondine-Ca prevails (Fig. 2b–d). Locally, rocks are enriched in minerals of the tobermorite, ettringite groups and unidentified opal-like Ca-hydrosilicates–phosphates.

In the contact facies of the paralava, needle-like inclusions of 1–2 μm in thickness of barringerite (Fig. 1c) and oldhamite are observed in diopside crystals. Small cracks in the rock ~0.1 mm in thickness are filled with aggregates of phosphides of the barringerite–transjordanite series replaced by murashkoite. Rare grains of Ti-bearing pyrrhotite, daubréelite and blue Ti^{3+}-bearing titanite were also noted.

A dark zone at the contact of the paralava with the altered country rock is characterised by zonation in the direction from paralava to country rock (Fig. 2b). The phosphide zone, where barringerite, transjordanite, murashkoite and zuktamrurite were identified, is gradually replaced by a phosphate zone. The phosphate zone consists mainly of minerals of the merrillite group and fluorapatite. Here, we identified graftonite-(Ca), $CaFe^{2+}_2(PO_4)_2$; crocobelonite, $CaFe^{3+}_2(PO_4)_2O$; Fe-analogue of stanfieldite, $Ca_4MgFe^{2+}_4(PO_4)_6$; and β-$Fe_2P_2O_7$ – a high-temperature analogue of nabateaite, γ-$Fe_2P_2O_7$, discovered recently in phosphide-bearing paralava in Israel (Britvin *et al.*, 2021c).

The phosphate zone is followed by a hematite zone, in which relics of Fe–Ni spinel and pyrrhotite are preserved, and on the boundary of which the country rock is transformed into chondrite-like rock (Fig. 2b). Individual diopside crystals are observed in all the described zones (Fig. 2b,c). Fe^{2+}-bearing phosphates tend to occur next to phosphides, whereas Fe^{3+}-bearing phosphates are usually in contact with hematite. Grained aggregates of deynekoite were found as intergrowths with hematite in several polished mounts. Typically, fluorapatite is intergrown with hematite (Fig. 2c,d). Small relics of Fe^{2+}-bearing phosphates and berlinite, $AlPO_4$, occurring in deynekoite deserve attention. The morphology of the hematite, which has a lattice-like form, indicates that it formed after the pyrrhotite crystals (Fig. 2d).

Deynekoite forms aggregates with grains up to 30–40 μm in size. The grains are transparent and light-yellow and light-brown in colour. The streak is white with a yellowish tint. The microhardness is VHN_{25} = 319(29), 253–331 (in kg/mm^2), which corresponds to a Mohs hardness of 4.5. The mineral is brittle with a conchoidal fracture, and cleavage is not observed. Its density, calculated on the basis of the empirical composition and the structural data, is 3.09 g·cm^{-3}. Deynekoite is uniaxial (–), its refractive indices are $\omega = 1.658(3)$, $\epsilon = 1.652(3)$ ($\lambda = 589$ nm), and pleochroism was not observed.

Deynekoite has a relatively invariable chemical composition (Tables 1, 3), and it can be described by the mean empirical formula $(Ca_{8.90}Na_{0.11}K_{0.02})_{\Sigma 9.03}(Fe^{3+}_{0.62}Mg_{0.30}Al_{0.05})_{\Sigma 0.97}P_{6.98}V^{5+}_{0.05}$

https://doi.org/10.1180/mgm.2023.71 Published online by Cambridge University Press

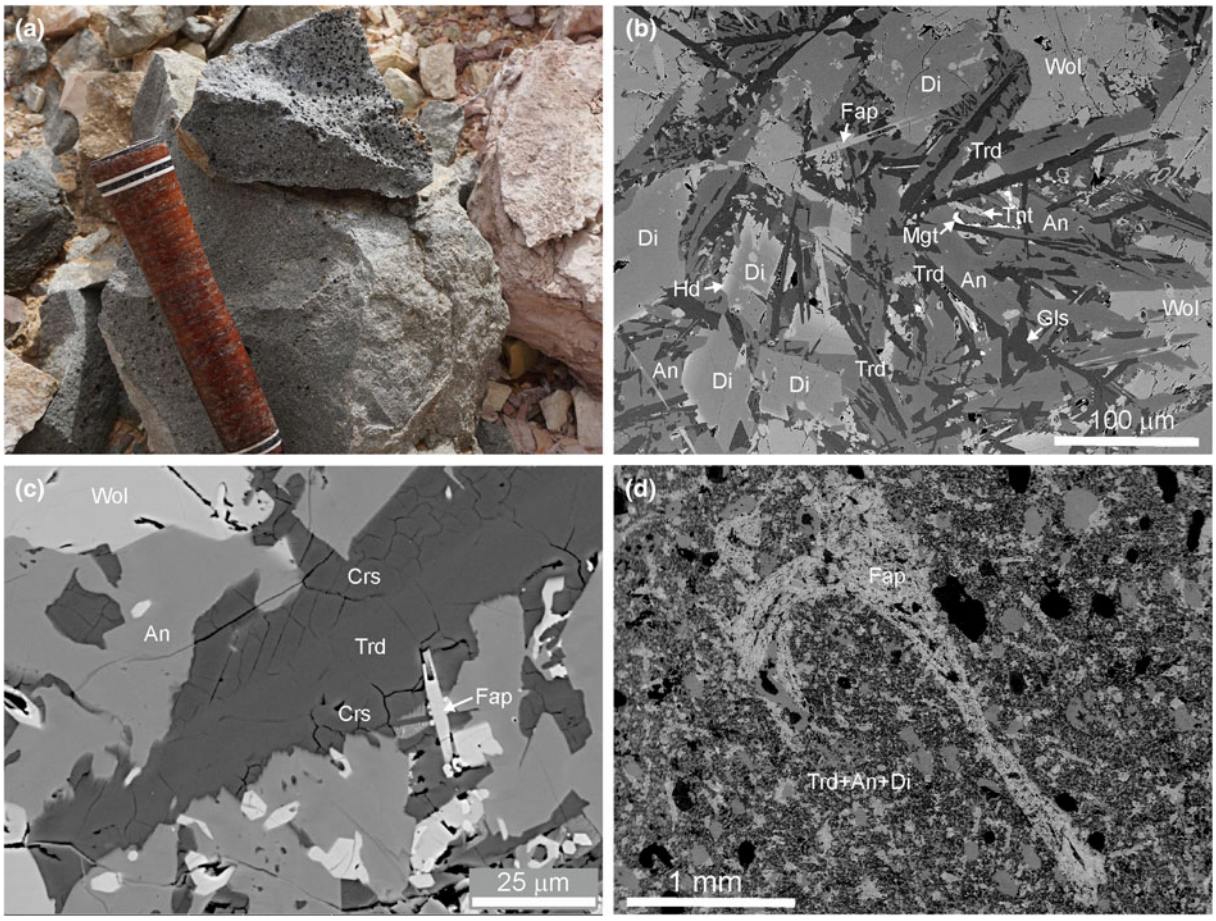

Figure 1. (a) Heterogeneous, porous basalt-like rock from a central part of the paralava body. (b) Paralava consisting of diopside, tridymite, anorthite and wollastonite. Back-scattered electron (BSE) image. (c) Cristobalite with fish-scale texture fissures overgrowing tridymite. BSE image. (d) Pseudomorph of fluorapatite after fish bone in the paralava. BSE image. An = anorthite, Crs = cristobalite, Di = diopside, Fap = fluorapatite, Hd = hedenbergite, Gls = glass, Mgt = magnetite, Trd = tridymite, Tnt = titanite, Wol = wollastonite.

$O_{27.70}(OH)_{0.30}$, which can be simplified to $Ca_{9.00}(Fe^{3+}_{0.70}Mg_{0.30})_{\Sigma 1.0}[(PO_4)_{6.70}(PO_3OH)_{0.3}]_{\Sigma 7}$, and the end-member formula $Ca_9Fe^{3+}(PO_4)_7$.

Raman spectroscopy

In the Raman spectrum of deynekoite (Fig. 3) most of the bands are related to vibrations in $(PO_4)^{3-}$ groups: bands in the range 1200–1000 cm^{-1} are connected with vibrations $\nu_3(PO_4)^{3-}$; 1000–900 cm^{-1} with $\nu_1(PO_4)^{3-}$; 550–630 cm^{-1} with $\nu_4(PO_4)^{3-}$; and 400–470 cm^{-1} with $\nu_2(PO_4)^{3-}$. Bands lower than 300 cm^{-1} are ascribed to vibrations of Ca–O and lattice vibrations. In the deynekoite spectrum there are two bands, at 934 cm^{-1} and 880 cm^{-1}, which have low intensity but appear in all its spectra. These bands are not noted in merrillite and keplerite spectra (Britvin *et al.*, 2021b). The band at 934 cm^{-1} is related to P–O vibrations in the PO_3OH group. The same band is observed in the spectrum of whitlockite (Jolliff *et al.*, 2006). The band at 880 cm^{-1} is connected with the $\nu_1(VO_4)^{3-}$ vibration. As has been shown for the pyromorphite–vanadinite series, even for a low content, when V^{5+} substitutes for P^{5+} at the tetrahedra, bands from the stretching vibration of V–O in $\nu_1(VO_4)^{3-}$ are clearly visible in the Raman spectra (Solecka *et al.*, 2018). The OH-group content in deynekoite is insignificant, so bands from O–H stretching vibrations within the characteristic range 3000–3700 cm^{-1} are not observed (Fig. 3).

Deynekoite structure

The crystal structure of deynekoite was solved in the *R*3*c* space group with a dual-space algorithm implemented in *Shelxt* (Sheldrick, 2015a). The model was refined with least-squares minimisation using *Shelxl* (Sheldrick, 2015b), with *Olex2* (Dolomanov *et al.*, 2009) as the graphical interface. Twinning by inversion was observed with two domains of 56:44 ratios. The occupancy of the *M* site in deynekoite was constrained to 1 and refined as Fe vs. Mg. Disorder in the $^{P1}PO_4$ tetrahedron was observed, where the *P*1 and O10 sites split into two parts, forming *P*1A, O10A and *P*1B, O10B groups of atoms. The occupancy of $^{P1}PO_4$ was constrained to 1 and the occupancies of the disordered atoms were refined as part 1 vs. part 2. The H10b atom was fixed at 0.96 Å from O10B in the direction of the O8 atom to form an H-bond interaction. The occupancy of H10b was refined together with *P*1B and O10B in the 'part 2' group of the disordered atoms. Experimental details and refinement data are summarised in Tables 2, 4–6. The crystallographic information file has been deposited with the Principal Editor of *Mineralogical Magazine* and is available as Supplementary material (see

https://doi.org/10.1180/mgm.2023.71 Published online by Cambridge University Press

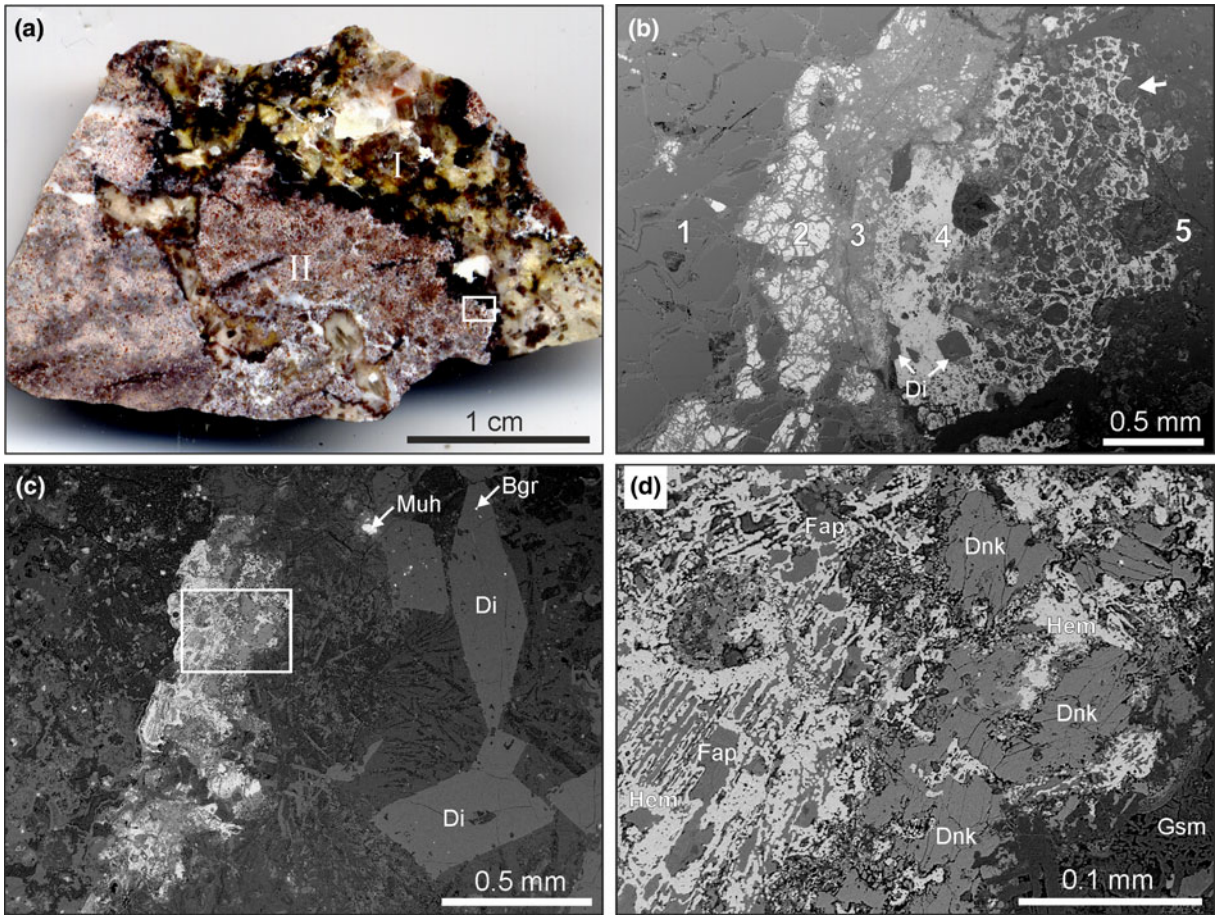

Figure 2. (a) Contact of diopside paralava (I) and altered marl (II), black is a hematite-bearing zone. The white frame shows a fragment magnified in Fig. 2b. (b) Position of phosphate mineralisation at the contact zone of rocks: 1 – diopside paralava, 2 – zone enriched with phosphides (murashkoite, zuktamrurite), 3 – phosphate zone, 4 – hematite zone (developed after pyrrhotite), 5 – altered host rock (marl); diopside chondrules are shown by arrows. (c) Phosphate zone represented, mainly, by deynekoite. Diopside paralava is replaced intensively by calcite and gismondine-Ca; in unaltered diopside crystals, barringerite inclusions are noted. The white frame shows a fragment magnified in Fig. 2d; (d) One of the rare places where deynekoite forms almost monomineralic aggregates of elongated grains up to 50 μm in size. Bgr = barringerite, Dnk = deynekoite, Di = diopside, Fap = fluorapatite, Hem = hematite, Gsm = gismondine-Ca, Muh = murashkoite.

below). In the deynekoite structure a series of polyhedra are distinguished, parts of which are fully occupied by cations of one type. There are tetrahedrally coordinated phosphorus sites P2 and P3, eight-coordinated Ca sites (Ca1, Ca2 and Ca3) and a number of oxygen sites (Table 4). The *M* site in minerals of the merrillite structure is always fully occupied (Britvin *et al.*, 2021b). In the case of deynekoite, this site is occupied by Fe^{3+}, Mg and Al. Refinement of the site occupation gave ($Fe^{3+}_{0.58}Mg_{0.42}$), which yields a charge of +2.58 and 20.12 e^-. Data from the microprobe analyses gave the occupation of the *M* site ($Fe^{3+}_{0.62}Mg_{0.30}Al_{0.05}$), which yields a charge of +2.61 and 20.37 e^-. Considering that it is impossible to separate Mg and Al during structure refinement, the data regarding the occupation of the *M* site are relevant to the microprobe analyses data, although it cannot be ruled out that the grain used for the structure refinement has a slightly lower Fe^{3+} content. The tetrahedral site *P*1 splits into sites *P*1A and *P*1B with refined occupation in a ratio of 0.73:0.27. The occupation ratio of the O10A and O10B sites is identical; the atoms are located at the top of the tetrahedra and oriented to the opposite sides. The bases of both tetrahedra are formed by oxygen O9–O9–O9. The tetrahedron $^{P1A}PO_4$ has the typical interatomic distances *P*1A–O9 = 1.534(4) Å and *P*1A–O10A = 1.526(14) Å (Table 6). The first variant of the structure refinement of deynekoite, submitted in the new-mineral proposal check-list, reported an anomalously large distance *P*1B–O10B = 1.78(5) Å and normal distances *P*1B–O9 = 1.517(6) Å×3. In whitlockite the distance *P*1B–(O10BH) ≈ 1.61 Å (Hughes *et al.*, 2008). The anomalous bond length may be due to the presence of a very small amount of Na at the *X* site, which overlaps with the O10B position in deynekoite. We have taken into consideration the *X* site in the revised deynekoite

Table 3. Chemical composition of deynekoite.

Wt.%	*n* = 12	S.D.	Range	Apfu
V_2O_5	0.41	0.17	0.07–0.72	0.05
P_2O_5	46.11	0.30	45.62–46.60	6.98
Fe_2O_3	4.59	0.19	4.20–4.88	0.62
Al_2O_3	0.25	0.08	0.16–0.42	0.05
CaO	46.40	0.20	46.02–46.82	8.90
MgO	1.14	0.09	1.00–1.31	0.30
K_2O	0.10	0.03	0.03–0.13	0.02
Na_2O	0.32	0.10	0.22–0.54	0.11
H_2O*	0.25			0.30**
Total	99.57			

* Water was calculated by charge balance; ** (OH) apfu; S.D. – standard deviation

https://doi.org/10.1180/mgm.2023.71 Published online by Cambridge University Press

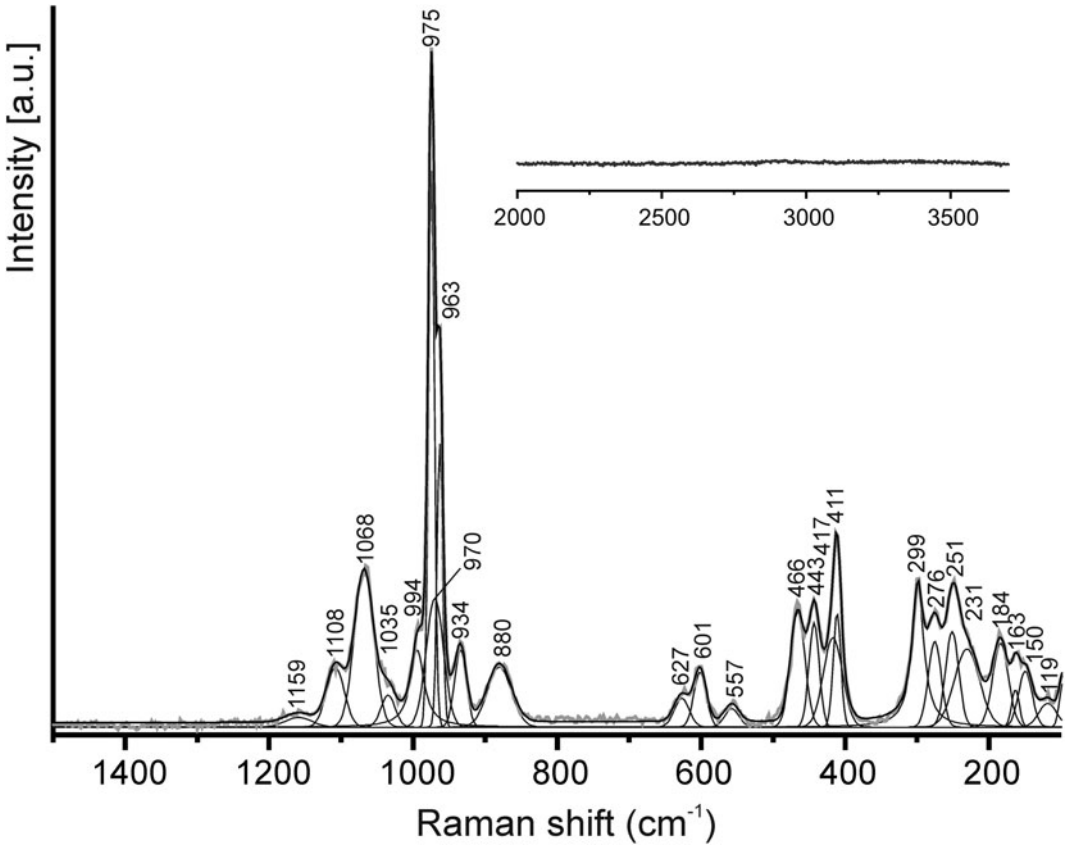

Figure 3. Raman spectrum of deynekoite.

structure model and have refined the Na content at this site equal to 0.1 atoms per formula unit (apfu). It may be that the *X* site has the lower occupation as it can contain K (Table 2). In the revised model, the distances in the $^{P1B}PO_4$ tetrahedron are *P*1B–O10B = 1.64(5) Å and *P*1B–O9 = 1.519(6) Å ×3 (Table 5). The increase in the *P*1B–O10B distance in comparison with *P*1A–O10A is connected with the partial protonation of O10B with the formation of strong hydrogen bond O10B···O8 with the distance $d_{O10B–O8}$ = 2.68(3)Å and $\angle^{O–H···O}$ = 175.5° (see Fig. 5e). The deynekoite structure, which is formed by the intercalation of two types of layers, is shown in Fig. 4.

As deynekoite occurs only in tiny amounts and its crystals contain large amounts of inclusions of other phases, powder

Table 4. Fractional atomic coordinates and isotropic* or equivalent isotropic displacement parameters (Å^2) for deynekoite.

Site	Occ. (<1)	*x*	*y*	*z*	U_{iso}*/U_{eq}
Fe1	0.576(10)	0.6667	0.3333	0.33484(8)	0.0045(6)
Mg1	0.424(10)	0.6667	0.3333	0.33484(8)	0.0045(6)
Ca1	1	0.61475(17)	−0.20227(15)	0.34205(4)	0.0150(3)
Ca2	1	0.20089(16)	−0.18755(16)	0.23520(4)	0.0080(3)
Ca3	1	0.71378(17)	0.87050(16)	0.43656(4)	0.0086(3)
P2	1	0.82550(19)	0.6837(2)	0.36583(5)	0.0058(4)
P3	1	0.5121(2)	−0.0113(2)	0.30356(5)	0.0067(4)
O1	1	0.4797(5)	−0.0511(6)	0.34325(13)	0.0156(12)
O2	1	0.6191(5)	−0.0638(5)	0.29028(13)	0.0097(10)
O3	1	0.3651(5)	−0.0804(5)	0.28267(13)	0.0106(11)
O4	1	0.5901(5)	0.1608(5)	0.29815(13)	0.0089(11)
O5	1	0.7514(5)	0.5083(5)	0.36891(13)	0.0075(10)
O6	1	0.9847(5)	0.7502(6)	0.38010(12)	0.0114(11)
O7	1	0.7262(5)	0.7235(5)	0.38869(12)	0.0073(10)
O8	1	0.8182(5)	0.7277(5)	0.32734(13)	0.0129(11)
O9	1	0.4804(5)	0.8012(5)	0.41180(15)	0.0129(12)
P1A	0.734(11)	⅓	⅔	0.39934(14)	0.0075(14)
Na7	0.10(2)	⅓	⅔	0.481(3)	0.03(3)*
O10A	0.734(11)	⅓	⅔	0.3583(4)	0.012(3)
P1B	0.266(11)	⅓	⅔	0.4229(4)	0.004(3)*
O10B	0.266(11)	⅓	⅔	0.4671(12)	0.021(12)*
H10B	0.089(4)	0.27(5)	0.70(7)	0.478(2)	0.031*

Table 5. Atomic displacement parameters (Å^2) for deynekoite.

	U^{11}	U^{22}	U^{33}	U^{23}	U^{13}	U^{12}
Fe1	0.0041(7)	0.0041(7)	0.0053(12)	0	0	0.0021(3)
Mg1	0.0041(7)	0.0041(7)	0.0053(12)	0	0	0.0021(3)
Ca1	0.0260(8)	0.0109(8)	0.0119(8)	−0.0016(7)	−0.0066(7)	0.0120(7)
Ca2	0.0073(7)	0.0073(7)	0.0084(8)	−0.0011(6)	−0.0011(7)	0.0028(6)
Ca3	0.0101(8)	0.0088(7)	0.0081(8)	−0.0018(7)	−0.0017(7)	0.0056(7)
P2	0.0047(10)	0.0049(8)	0.0069(11)	0.0008(8)	0.0008(8)	0.0018(7)
P3	0.0052(8)	0.0070(8)	0.0078(10)	−0.0014(8)	−0.0015(9)	0.0031(8)
O1	0.015(3)	0.030(3)	0.008(3)	0.001(2)	0.000(2)	0.016(2)
O2	0.014(2)	0.010(2)	0.009(3)	0.002(2)	0.001(2)	0.009(2)
O3	0.007(2)	0.012(2)	0.009(3)	−0.002(2)	−0.004(2)	0.002(2)
O4	0.012(3)	0.005(2)	0.012(3)	−0.003(2)	0.001(2)	0.006(2)
O5	0.006(2)	0.007(2)	0.008(3)	0.0008(19)	0.001(2)	0.002(2)
O6	0.009(2)	0.014(2)	0.010(3)	0.000(2)	0.000(2)	0.005(2)
O7	0.008(2)	0.007(2)	0.007(3)	0.001(2)	0.002(2)	0.004(2)
O8	0.014(3)	0.015(3)	0.007(3)	0.000(2)	0.001(2)	0.006(2)
O9	0.004(2)	0.009(2)	0.022(3)	0.004(2)	−0.001(2)	0.0013(17)
P1A	0.0044(13)	0.0044(13)	0.014(4)	0	0	0.0022(7)
O10A	0.012(4)	0.012(4)	0.012(7)	0	0	0.006(2)

https://doi.org/10.1180/mgm.2023.71 Published online by Cambridge University Press

Table 6. Selected bond lengths (Å) and bond-valence sum (BVS) calculation for deynekoite.

Fe1–O4	2.064(5)	×3	Ca3–O8	2.368(5)	
Fe1–O5	2.016(5)	×3	Ca3–O9	2.338(5)	
BVS Fe^{3+}	2.81		Mean	2.471	
BVS Mg^{2+}	2.26		BVS	2.12	
BVS Fe^{2+}	2.63				
BVS $Fe^{3+}_{0.58}Mg_{0.42}$	2.58		P2–O5	1.583(5)	
Mean	2.040		P2–O6	1.529(5)	
			P2–O7	1.540(5)	
Ca1–O1	2.568(5)		P2–O8	1.514(5)	
Ca1–O1	2.488(5)		Mean	1.5415	
Ca1–O2	2.386(5)		BVS	4.92	
Ca1–O3	2.655(5)				
Ca1–O6	2.448(5)		P3–O1	1.523(6)	
Ca1–O7	2.411(5)		P3–O2	1.539(5)	
Ca1–O8	2.605(5)		P3–O3	1.530(5)	
Ca1–O9	2.950(6)		P3–O4	1.558(5)	
Ca1–O10A	2.596(3)		Mean	1.5375	
Mean	2.567		BVS	4.96	
BVS	1.93				
			P1A–O9	1.534(4)	×3
Ca2–O1	2.377(5)		P1A–O10A	1.526(14)	
Ca2–O2	2.470(5)		Mean	1.532	
Ca2–O3	2.312(5)		BVS	5.03	
Ca2–O5	2.492(5)				
Ca2–O5	2.517(5)		P1B–O9	1.519(6)	×3
Ca2–O6	2.746(5)		P1B–O10B	1.64(5)	
Ca2–O7	2.491(5)		Mean	1.549	
Ca2–O9	2.427(5)		BVS	4.85	
Mean	2.479				
BVS	2.10		Na–O8	2.532(18)	×3
			Na–O9	2.96(8)	×3
Ca3–O2	2.619(5)		Mean	2.746	
Ca3–O3	2.628(5)		BVS	0.55	
Ca3–O4	2.461(5)				
Ca3–O4	2.489(5)		H10B	0.96(3)	
Ca3–O6	2.477(5)		BVS	0.99	
Ca3–O7	2.386(5)				

X-ray diffraction data were not collected, as it could be calculated more reliably from the results of single-crystal structure refinements. The calculated data are listed in Supplementary Table S1.

Discussion

Nomenclature problems

The cerite supergroup combines two groups, cerite and merrillite, of which the latter is divided into two more subgroups: merrillite and whitlockite (Atencio and Azzi, 2020). An archetype of the phosphate structure of the merrillite group is β-$Ca_3(PO_4)_2$ (Z = 21, $R3c$ (#161), a ≈ 10.35Å, c ≈ 37.16 Å; Sugiyama and Tokonami, 1987), which in turn is a stable, low-pressure polymorph of the mineral tuite, γ-$Ca_3(PO_4)_2$ (Z = 3, $R\bar{3}m$, a ≈ 5.26 Å, c ≈ 18.73 Å; Xie *et al.*, 2003).

The general formula of minerals of the cerite supergroup is as follows: $A_9XM[TO_3Ø]_7W_3$, where A = Ce, La, Ca, Sr, (Na), (other REE); X = □ [vacancy], Ca and Na; M = Mg, Fe^{2+}, Fe^{3+}, Al and Mn; T = Si and P; Ø = O and OH; W = □, OH and F (Atencio and Azzi, 2020). The known minerals of the merrillite group have simpler formulae as the W site is absent: $A_9XM(TO_4)_3(TO_3Ø)_4$. β-$Ca_3(PO_4)_2$ is not known in Nature, and its formula as a potential member of the merrillite group can be written as $Ca_9(Ca_{0.5}□_{0.5})Ca(PO_4)_7$ (Z = 6). Deynekoite, $Ca_9□Fe^{3+}(PO_4)_7$, is the first mineral of the merrillite group with Fe^{3+} at the M octahedral site and a vacant X site (Table 1). Deynekoite has unit cell parameters close to the parameters of other minerals of the merrillite subgroup (Supplementary Table S2). The refractive indexes and birefringence for deynekoite are higher than for other known minerals of the merrillite subgroup (Supplementary Table S2).

The recently approved classification of the cerite supergroup was intended to solve a problem with the unification of mineral formulas of the merrillite group (see the IMA formula in Table 1). The authors of the new classification (Atencio and Azzi, 2020) propose the use of generalised formulas employing the sign "#" to replace minor chemical elements that balance the charge. For example, merrillite would have the formula $(Ca,\#)_9(Na,\#)(Mg,\#)(PO_4)_7$, keplerite $(Ca,\#)_9(Ca,\#)(Mg,\#)(PO_4)_7$ and hedegaardite $(Ca,\#)_9(Ca,\#)(Mg,\#)[PO_3(OH)](PO_4)_6$. Using the approach of Atencio and Azzi (2022), deynekoite would be described by the formula $(Ca,\#)_9(□,\#)(Fe^{3+},\#)(PO_4)_7$. Apparently, this approach does not include end-member formulas with a double site occupation at the one site (keplerite and matyhite, Table 1). Thus, the principles of mineral systematics (Bosi *et al.*, 2019a, 2019b) based on the definition of the end-member formula may not be fulfilled.

Furthermore, with the nomenclature proposed by Atencio and Azzi (2020), keplerite, $(Ca,\#)_9(Ca,\#)(Mg,\#)(PO_4)_7$, and hedegaardite, $(Ca,\#)_9(Ca,\#)(Mg,\#)[PO_3(OH)](PO_4)_6$, are distinguished by only one hydrogen atom (~0.85% wt. H_2O). As a result, these formulas will not help to identify these mineral species on the basis of routine microprobe analyses. However, using the specific formulas of the end-members hedegaardite and keplerite (Table 1) makes the identification of minerals of the cerite supergroup relatively simply. We believe that the classification of the cerite supergroup may be improved by taking these issues into account.

Structural aspects

The crystal structure of the merrillite-group minerals is formed by a framework of cation-centred polyhedra linked by common corners and edges. There are PO_4 tetrahedra, MO_6 octahedra, AO_8 polyhedra and XO_6 distorted trigonal prisms. The merrillite type structure is usually considered a combination of columns of different types along the Z axis (Britvin *et al.*, 2021b). It can also be described as an interlayering of corrugated layers (modules) of two types, nested within each other (Fig. 4, 5). This interpretation was applied, for example, in the description of the structure of $Ca_9Y(VO_4)_7$ (Lazoryak *et al.*, 2018).

The first type of layer (type *B*, Fig. 4) is presented by corrugated six-fold rings formed by the edge sharing $^{A}CaO_8$ polyhedra. In the inside ring in the merrillite layer there is a truncated $^{X}NaO_6$ prism, sharing common edges with Ca polyhedra (Fig. 5a). The prism also shares a top face with $^{P1A}PO_4$ tetrahedra and bottom corners with three other phosphate groups, which are linked to the Ca ring apically (Fig. 5c). In deynekoite, an Na(X) site has low occupation (0.1 apfu) and inside the ring there is a virtual trigonal bipyramid (Fig. 5a) which is formed by a disordered PO_4 tetrahedron oriented either down ($^{P1A}PO_4$) or up ($^{P1B}PO_4$) in the ratio 0.73:0.27 (Fig. 5d,e). As a rule, in minerals of the merrillite subgroup the $^{P1A}PO_4$ tetrahedron is occupied (at the top of the truncate Na-prism), whereas in the whitlockite-subgroup minerals, the $^{P1B}PO_4$ tetrahedron is practically fully occupied (at the place of the missing Na-site) (Figs 5c, 6). In a synthetic phase, which is very close in composition to natural deynekoite (Deyneko *et al.*, 2014), the tetrahedron-up $^{P1B}PO_4$ is fully

https://doi.org/10.1180/mgm.2023.71 Published online by Cambridge University Press

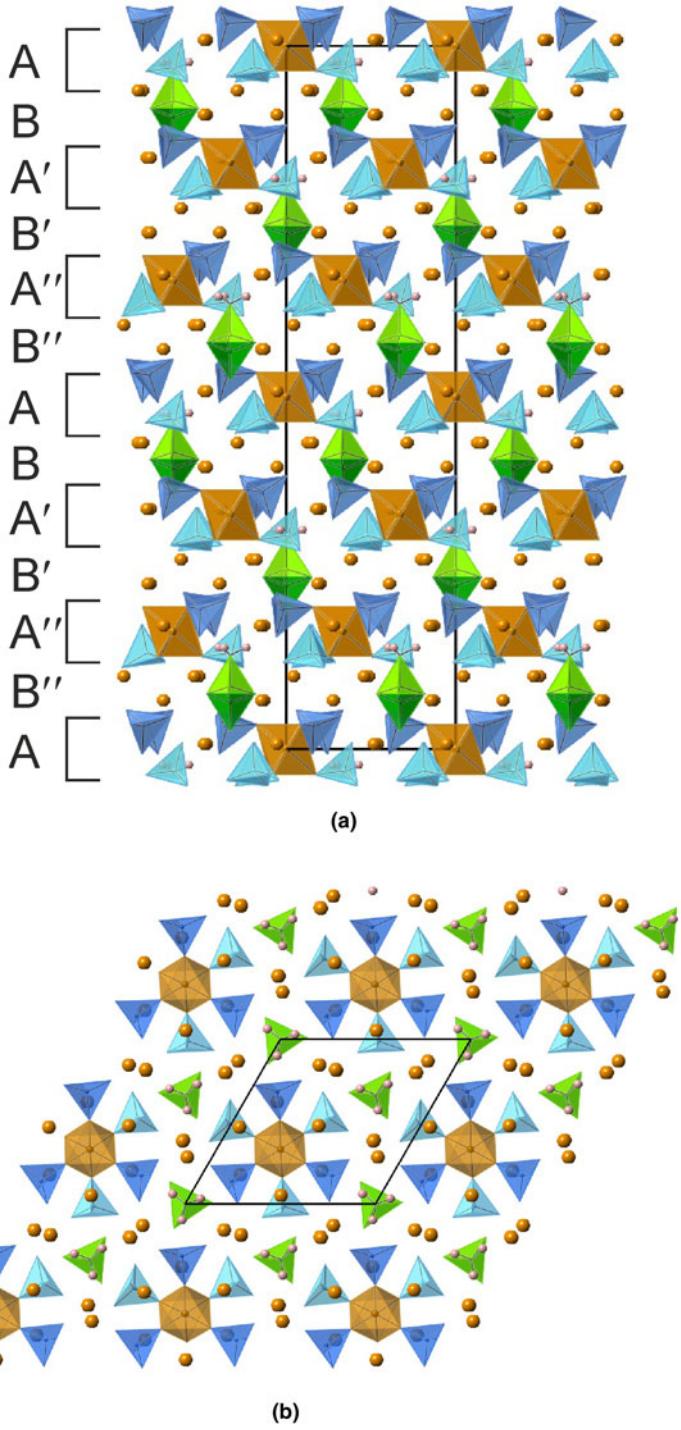

Figure 4. Deynekoite structure. (a) Projection on (010). The structure can be presented as the intercalation of two types of layers (see Fig. 5) in the sequence *ABA'B'A''B''A*. (b) Projection on (001). One slice of the *A* layer and two slices of *B* layers are shown. The Na site with lower occupation is not shown. Ca atoms – light-orange; Na atoms – yellow; $^{P2}PO_4$ tetrahedron – dark-blue; $^{P3}PO_4$ tetrahedron – blue; $^{P1A}PO_4$ tetrahedron – dark-green; $^{P1B}PO_4$ tetrahedron – light-green; MO_6 octahedron – brown; oxygen O10B – dark blue balls; oxygen O10A – blue balls; hydrogen – small pink balls.

occupied as in whitlockite (Figs. 5e, 6). However, in whitlockite the tetrahedron-down $^{P1A}PO_4$ can have a low phosphorus content (Fig. 6d). The second type of structural layer (*A* type, Fig. 4) repeats without changes in all minerals of the merrillite group and features $M(PO_4)_6$ clusters. The clusters are linked to each other by Ca-polyhedra (CaO_8) triplets (Fig. 5b).

Deynekoite is the first mineral of the merrillite group with a formally vacant *X* (Na) site (Na pfu ≤ 0.1). Natural deynekoite, $\sim Ca_9(\square_{0.9}Na_{0.1})[Fe^{3+}_{0.58}(Mg,Al)_{0.42}](P\ O_4)_{6.73}(PO_3OH)_{0.27}$, has a synthetic analogue with close composition – $Ca_9(Fe^{3+}_{0.63}Mg_{0.37})(PO_4)_{6.63}(PO_3OH)_{0.37}$ (Deyneko *et al.*, 2014). In the synthetic analogue the tetrahedron-up $^{P1B}PO_4$ with apical oxygen, which is partially (0.37) protonated, is fully occupied (Fig. 6b). In deynekoite the tetrahedron-down $^{P1A}PO_4$ has 0.73 occupation, vs. 0.27 for the tetrahedron-up $^{P1B}PO_4$ (Fig. 6a). The apical oxygen ^{O10B}O of $^{P1B}PO_4$ forms an OH group, where ^{H10B}H is disordered between three symmetrically equivalent positions. The distance $^{P1B}P–^{O10B}O = 1.64$ Å is increased compared to the distance $^{P1B}P–^{O10B}O = 1.53$ Å (Table 6) and close to the distance $^{P1B}P–^{O10B}O = 1.614$ Å in whitlockite (Hughes *et al.*, 2008).

https://doi.org/10.1180/mgm.2023.71 Published online by Cambridge University Press

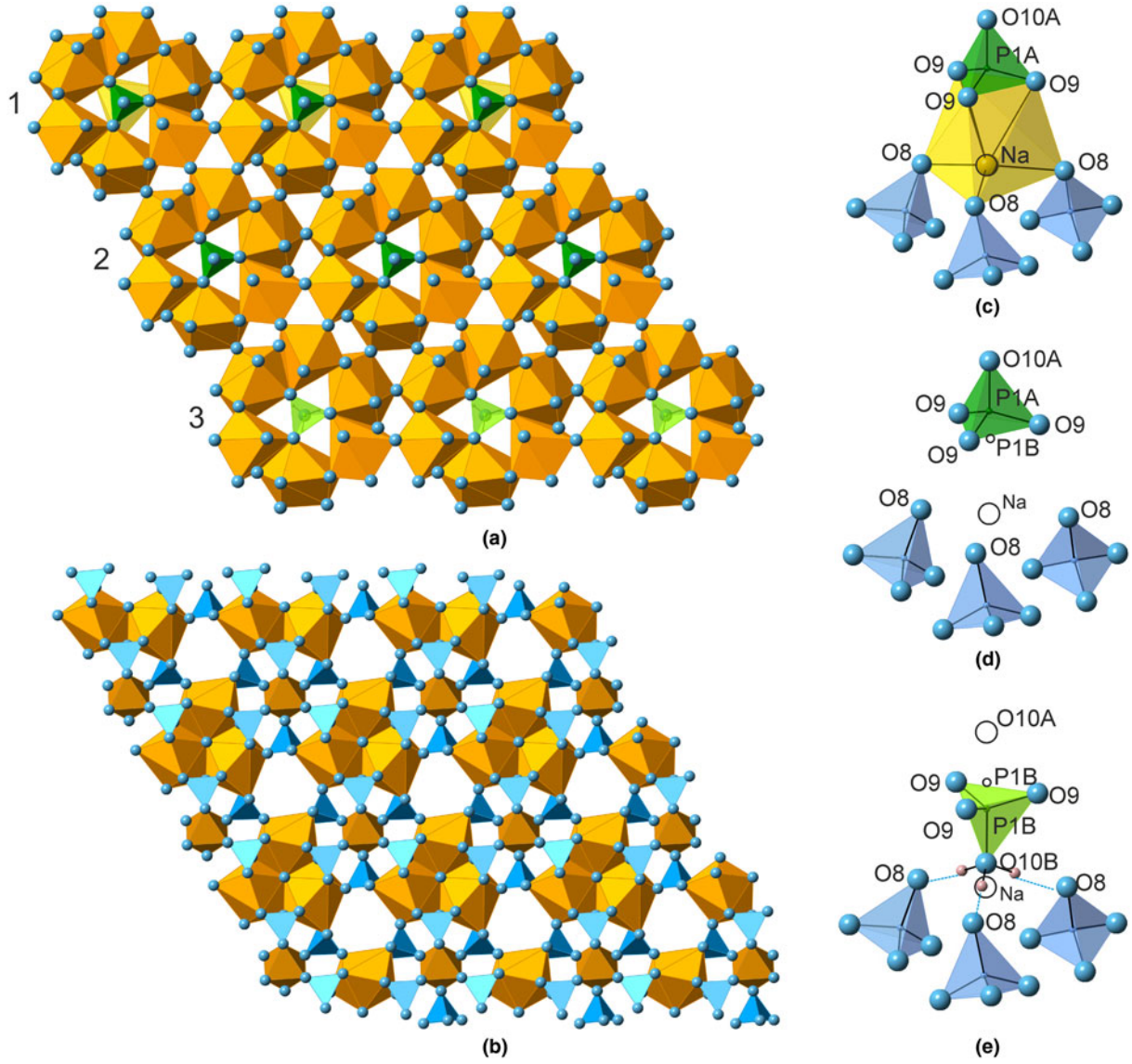

Figure 5. (a,b) Layers of two types (*A*, *B* see Fig. 4) in the structure of deynekoite, projection on (00$\bar{1}$). (a) In the *B* layer formed by six-membered rings building from Ca-polyhedra, three types of triangular empty occupation are shown as in the ideal structures of merrillite (1), deynekoite (2) and whitlockite (3). (b) The *A* layer is the same in merrillite, deynekoite and whitlockite, consisting of millwheel clusters $M(^{P2+P3}PO_4)_6$ linked with one another by triplets of Ca-polyhedra. (c–e) Atom arrangement near the *P*1 site in holotype deynekoite: c – merrillite type (10%); d – deynekoite type (63%); e – whitlockite type (27%). Ca-polyhedra – light-orange; $^{P2}PO_4$ tetrahedron – dark-blue; $^{P3}PO_4$ tetrahedron – blue; $^{P1A}PO_4$ tetrahedron – dark-green; $^{P1B}PO_4$ tetrahedron – light-green; truncated prism XO_6 – yellow; octahedron MO_6 – brown (Fe3+)/dark-orange (Mg); oxygen – blue balls; hydrogen – pink balls (hydrogen bonds are shown); empty circle – vacancy.

The iron valence in deynekoite was not determined by the direct method because of the limited amount of material and very small grain size. The yellow-to-brown colour of deynekoite, totals from microprobe analyses close to 100% and the significant decrease of the mean *M*–O = 2.041 Å in comparison with other minerals of the merrillite group (which have the distance *M*–O = 2.08 Å) all indicate that iron in deynekoite is trivalent. This is confirmed by the bond-valence sum (BVS) calculation (Table 5), which shows that the trivalent cation predominates at the *M* site.

The differences in the occupation of the $^{P1}(PO_4)^{3-}$ sites in deynekoite and synthetic analogues can be explained by the peculiar features of deynekoite's origin. Initially, in high-temperature and reduced conditions, ferromerrillite, $NaCa_9(Fe^{2+},Mg)(PO_4)_7$, forming a solid solution with keplerite, $Ca_{0.5}Ca_9(Fe^{2+},Mg)(PO_4)_7$, crystallises. As the temperature decreases and oxygen activity increases, ferromerrillite is replaced by deynekoite with the removal of Na from the structure. Deynekoite inherits the characteristics of the ferromerrillite structure – the $^{P1A}PO_4$ tetrahedron preserves significant occupation, though a small part of the phosphorus changes its position and occupies the $^{P1B}PO_4$ site, accompanied by the protonation of the ^{O10B}O apical oxygen.

Genesis

Diopside–anorthite–tridymite paralava, on the contact of which deynekoite was found, was generated at the near-surface combustion focus. This was a continuous and relatively long-lasting combustion phenomenon that determined the anomalous high temperature of the generated melt (~1500°C). One indicator of

https://doi.org/10.1180/mgm.2023.71 Published online by Cambridge University Press

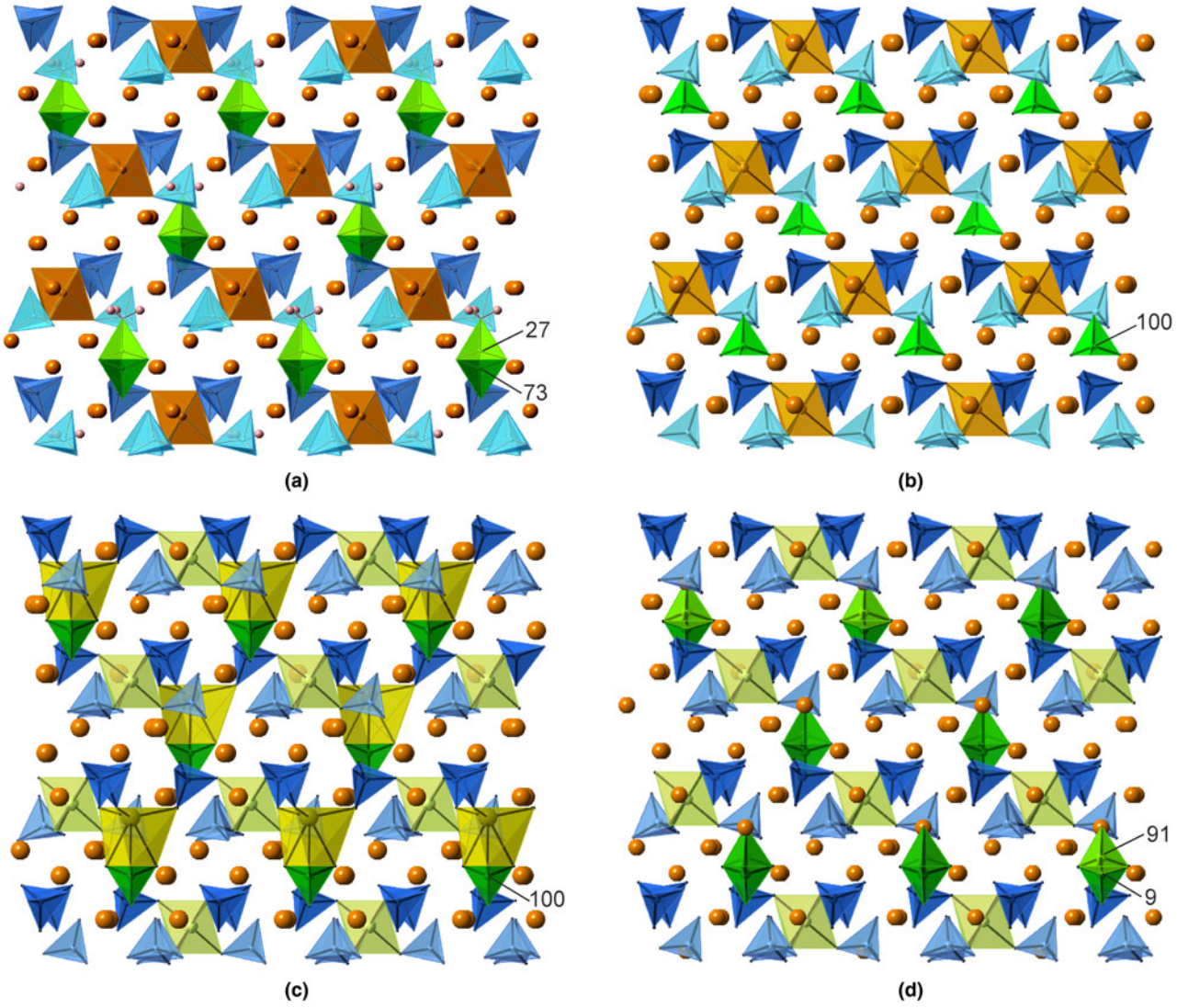

Figure 6. Comparison of deynekoite [(a), Na site lower occupied is not shown] and its synthetic analogue [(b), crystal structure data from Deyneko *et al.*, 2014], merrillite [(c), crystal structure data from Xie *et al.*, 2015] and whitlockite [(d), crystal structure data from Hughes *et al.*, 2008], projection on (010). Ca – light-orange balls; $^{P2}PO_4$ tetrahedron – dark blue; $^{P3}PO_4$ tetrahedron – blue; $^{P1A}PO_4$ tetrahedron – dark-green; $^{P1B}PO_4$ tetrahedron – light-green; truncate prism XO_6 – yellow; MO_6 octahedron – brown (Fe)/light-green (Mg); hydrogen – pink balls. The numerals show tetrahedral site occupation in percent.

the super-high combustion temperature is cristobalite with a fish-scale or ballen structure (Fig. 1c), which reflects volume shrinkage upon the inversion of β-cristobalite to α-cristobalite (Schmieder *et al.*, 2009).

The genesis of phosphides and phosphates on the boundary of the diopside–anorthite–tridymite paralava was connected with the interaction of the paralava and country rocks, which were a source of reductant (altered bitumen) and also phosphorus and iron. These probably came from the phosphorite-bearing rocks of the Muwaqqar formation, the so-called P–Fe–C (± Si) series analogous to the rocks of the lower part of the Ghareb formation, Israel (Shahar *et al.*, 1989). A find of fluorapatite pseudomorphs after fish bones in the paralava confirms the presence of phosphorite inclusions in the carbonate protolith (Fig. 1d). Accessory fluorapatite in the paralava was stable on the contact of paralava with the country rocks and cannot be a source of phosphorus. The genesis of phosphides is related to carbothermal reductive reactions on the boundary of paralava and country rocks. These reactions were considered by us in the frame of the phosphide genesis model defined for the contact of gehlenite paralava and fragments of country rocks in breccia of the Hatrurim Basin in the Negev Desert, Israel: $Fe_2O_3 + 3C \rightarrow 2Fe(lq) + 3CO(g)$; $8Ca_5(PO4)_3F$ [fluorapatite from phosphorite with $(OH)^-$ and $(CO_3)^{2-}$ impurities] $+ 22SiO_2 + 20Al_2O_3 + 60C = 12P_2(g) + 60CO(g) + 20Ca_2Al_2O_7 + 2SiF_4(g)$; $nFe(lq) + ½P_2(g) = FenP$, $n = 1,2,3$ (Galuskin *et al.*, 2022a, 2023b). The crystallisation of phosphides took place in the context of the increasing activity of P that is reflected in the crystallisation sequence of Fe_2P (barringerite) – FeP (murashkoite) – FeP_2 (zuktamrurite) (Britvin *et al.*, 2019a, 2019b). The temperature of phosphide formation from a melt was higher than 1300°C (the temperature of barringerite crystallisation is 1350°C), which is similar to the temperature at which troilite (pyrrhotite) crystallises from sulfide melt. With the further decrease in temperature and increasing influence of atmospheric oxygen (processes occurring at near-surface conditions), phosphides were replaced by Fe^{2+}-bearing phosphates, which were changed by association of Fe^{3+}-bearing phosphates. Our investigations of phosphide-bearing rocks from

https://doi.org/10.1180/mgm.2023.71 Published online by Cambridge University Press

Jordan and Israel show that other minerals of the merrillite group (merrillite, keplerite, ferromerrillite and possibly matyhite), also appear in them. These minerals contain Fe^{2+} and crystallise from the locally generated phosphate melt at high temperatures (~1200°C). Deynekoite, which contains Fe^{3+} (substituting Fe^{2+}-phosphates) and a small amount of water (see below), was formed at lower temperatures (600–800°C). Most likely, when the early associations were replaced by later ones, metasomatic mechanisms of the replacement of minerals in the quasi-solid state and with the participation of intergranular melt and active gases were realised.

Acknowledgements. The authors thank Peter Leverett and two anonymous reviewers for their useful and constructive comments. Investigations were supported by the National Science Center of Poland Grant (grant number 2021/41/B/ST10/00130).

Supplementary material. The supplementary material for this article can be found at https://doi.org/10.1180/mgm.2023.71.

Competing interests. The authors declare none.

References

Atencio D. and Azzi A. (2020) Cerite: A new supergroup of minerals and cerite-(La) renamed ferricerite-(La). *Mineralogical Magazine*, **84**, 928–931.

Benarafaa A., Kacimia M., Gharbagea S., Millet J.-M. and Ziyada M. (2000) Structural and spectroscopic properties of calcium-iron $Ca_9Fe(PO_4)_7$ phosphate. *Materials Research Bulletin*, **35**, 2047–2055.

Bentor Y.K. (editor) (1960) Israel. In: *Lexique Stratigraphique International, Asie, Vol. III, (10.2)*. Centre national de la recherche scientifique, Paris.

Bosi F., Biagioni C. and Oberti R. (2019a) On the chemical identification and classification of minerals. *Minerals*, **9**, 591.

Bosi F., Hatert F., Hålenius U., Pasero M., Miyawaki R. and Mills S. (2019b) On the application of the IMA–CNMNC dominant-valency rule to complex mineral compositions. *Mineralogical Magazine*, **83**, 627–632.

Britvin S.N., Pakhomovskii Y.A., Bogdanova A.N. and Skiba V.I. (1991) Strontiowhitlockite, $Sr_9Mg(PO_3OH)(PO_4)_6$, a new mineral species from the Kovdor deposit, Kola Peninsula, U.S.S.R. *The Canadian Mineralogist*, **29**, 87–93.

Britvin S.N., Krivovichev S.V. and Armbruster T. (2016) Ferromerrillite, $Ca_9NaFe^{2+}(PO_4)_7$, a new mineral from the Martian meteorites, and some insights into merrillite-tuite transformation in shergottites. *European Journal of Mineralogy*, **28**, 125–136.

Britvin S.N., Murashko M.N., Vapnik Ye., Polekhovsky Yu.S., Krivovichev S.V., Vereshchagin O.S., Vlasenko N.S., Shilovskikh V.V. and Zaitsev A.N. (2019a) Zuktamrurite, FeP_2, a new mineral, the phosphide analogue of löllingite, $FeAs_2$. *Physics* and *Chemistry* of *Minerals*, **46**, 361–369.

Britvin S.N., Vapnik Ye., Polekhovsky Yu.S., Krivovichev S.V., Krzhizhanovskaya M.G., Gorelova L.A., Vereshchagin O.S., Shilovskikh V.V. and Zaitsev AN (2019b) Murashkoite, FeP, a new terrestrial phosphide from pyrometamorphic rocks of the Hatrurim Formation, Southern Levant. *Mineralogy and Petrology*, **113**, 237–248.

Britvin S.N., Murashko M.N., Vapnik Ye., Polekhovsky Yu.S., Krivovichev S.V., Krzhizhanovskaya M.G., Vereshchagin O.S., Shilovskikh V.V. and Vlasenko N.S. (2020) Transjordanite, Ni_2P, a new terrestrial and meteoritic phosphide, and natural solid solutions barringerite–transjordanite (hexagonal Fe_2P–Ni_2P). *American Mineralogist*, **105**, 428–436.

Britvin S.N., Murashko M.N., Krzhizhanovskaya M.G., Vapnik Ye., Vlasenko N.S., Vereshchagin O.S., Pankin D.V. and Vasiliev E.A. (2021a) Moabite, IMA 2020–092. CNMNC Newsletter 60; *Mineralogical Magazine*, **85**, 454–458.

Britvin S.N., Galuskina I.O., Vlasenko N.S., Vereshchagin O.S., Bocharov V.N., Krzhizhanovskaya M.G., Shilovskikh V.V., Galuskin E.V., Vapnik Ye. and Obolonskaya E.V. (2021b) Keplerite, $Ca_9(Ca_{0.5}\square_{0.5})Mg(PO_4)_7$, a new meteoritic and terrestrial phosphate isomorphous with merrillite, $Ca_9NaMg(PO_4)_7$. *American Mineralogist*, **106**, 1917–1927.

Britvin S.N., Murashko M.N., Vapnik Ye., Vlasenko N.S., Vereshchagin O.S., Krzhizhanovskaya M.G. and Bocharov V.N. (2021c) Nabateaite, IMA 2021–026. CNMNC Newsletter 62; *Mineralogical Magazine*, **85**, 634–638.

Britvin S.N., Murashko M.N., Vapnik Ye., Zaitsev A.N., Shilovskikh V.V., Krzhizhanovskaya M.G., Gorelova L.A., Vereshchagin O.S., Vasilev E.A. and Vlasenko N.S. (2022a) Orishchinite, a new terrestrial phosphide, the Ni-dominant analogue of allabogdanite. *Mineralogy and Petrology*, **116**, 369–378.

Britvin S.N., Murashko M.N., Krzhizhanovskaya M.G., Vereshchagin O.S., Vlasenko N.S., Vapnik Ye. and Bocharov V.N. (2022b) Nazarchukite, IMA 2022-005, in: CNMNC Newsletter 67. *Mineralogical Magazine*, **86**, 849–853.

Britvin S.N., Murashko M.N., Krzhizhanovskaya M.G., Vlasenko N.S., Vereshchagin O.S., Vapnik Ye. and Bocharov V.N. (2023a) Crocobelonite, $CaFe_2^{3+}(PO_4)_2O$, a new oxyphosphate mineral, the product of pyrolytic oxidation of natural phosphides. *American Mineralogist*, **108**, 1973–1983.

Britvin S.N., Murashko M.N., Krzhizhanovskaya M.G., Vapnik Ye., Vlasenko N.S., Vereshchagin O.S., Pankin D.V., Zaitsev A.N. and Zolotarev A.A. (2023b) Yakubovichite, $CaNi_2Fe^{3+}(PO_4)_3$, a new nickel phosphate mineral of non-meteoritic origin. *American Mineralogist*, **108**, 2142–2150.

Cooper M.A., Hawthorne F.C., Abdu Y., Ball N.A., Ramik R.A. and Tait K.T. (2013) Wopmayite, ideally $Ca_6Na_3Mn(PO_4)_3(PO_3OH)_4$, a new phosphate mineral from the Tanco Mine, Bernic Lake, Manitoba. *The Canadian Mineralogist*, **51**, 93–106.

Deyneko D.V., Aksenov S.M., Morozov V.A., Stefanovich S.Yu., Dimitrova O.V., Barishnikova O.V. and Lazoryak B.I. (2014) A new hydrogen-containing whitlockite-type phosphate $Ca_9(Fe_{0.63}Mg_{0.37})H_{0.37}(PO_4)_7$: hydrothermal synthesis and structure. *Zeitschrift für Kristallographie*, **229**, 823–830.

Dolomanov O.V., Bourhis L., Gildea R.J., Howard J.A.K. and Puschmann H. (2009) OLEX2: a complete structure solution, refinement and analysis program. *Journal* of *Applied Crystallography*, **42**, 339–341.

Frondel C. (1943) Mineralogy of the calcium phosphates in insular phosphate rock. *American Mineralogist*, **28**, 215–232.

Galuskin E.V., Gfeller F., Galuskina I.O., Pakhomova A., Armbruster T., Vapnik Y., Włodyka R., Dzierżanowski P. and Murashko M. (2015) New minerals with a modular structure derived from hatrurite from the pyrometamorphic Hatrurim Complex. Part II. Zadovite, $BaCa_6[(SiO_4)(PO_4)](PO_4)_2F$ and aradite, $BaCa_6[(SiO_4)(VO_4)](VO_4)_2F$, from paralavas of the Hatrurim Basin, Negev Desert, Israel. *Mineralogical Magazine*, **9**, 1073–1087.

Galuskin E.V., Galuskina I.O., Gfeller F., Krüger B., Kusz J., Vapnik Ye., Dulski M. and Dzierżanowski P. (2016) Silicocarnotite, $Ca_5[(SiO_4)(PO_4)](PO_4)$, a new 'old' mineral from the Negev Desert, Israel, and the ternesite–silicocarnotite solid solution: indicators of high-temperature alteration of pyrometamorphic rocks of the Hatrurim Complex, Southern Levant. *European Journal of Mineralogy*, **28**, 105–123.

Galuskin E.V., Krüger B., Galuskina I.O., Krüger H., Vapnik Ye., Pauluhn A. and Olieric V. (2019) Levantite, $KCa_3(Al_2Si_3)O_{11}(PO_4)$, a new latiumite-group mineral from the pyrometamorphic rocks of the Hatrurim Basin, Negev Desert, Israel. *Mineralogical Magazine*, **83**, 713–721.

Galuskin E., Galuskina I., Krüger B., Krüger H., Vapnik Ye., Krzątała A., Środek D. and Zieliński G. (2021) Nomenclature and classification of the arctite supergroup. Aravaite, $Ba_2Ca_{18}(SiO_4)_6[(PO_4)_3(CO_3)]F_3O$, a new arctite supergroup mineral from Negev Desert, Israel. *The Canadian Mineralogist*, **59**, 191–209.

Galuskin E.V., Galuskina I.O., Kamenetsky V., Vapnik Ye., Kusz J. and Zieliński G. (2022a) First *in-situ* terrestrial osbornite (TiN) in the pyrometamorphic Hatrurim Complex, Israel. *Lithosphere*, 81277447.

Galuskin E., Stachowicz M., Galuskina I.O., Woźniak K., Vapnik Y., Murashko N.N. and Zieliński G. (2022b) Deynekoite, IMA 2021-108. CNMNC Newsletter 66. *Mineralogical Magazine*, 86, https://doi.org/10.1180/mgm.2022.33

Galuskin E.V., Galuskina I.O., Vapnik Y. and Zieliński G. (2023a) Discovery of "meteoritic" layered disulphides $ACrS_2$ (A = Na, Cu, Ag) in terrestrial rock. *Minerals*, **13**, 381.

Galuskin E.V., Kusz J., Galuskina I.O., Książek M., Vapnik Ye. and Zieliński G. (2023b) Discovery of terrestrial andreyivanovite, FeCrP, and the effect of Cr

and V substitution in barringerite-allabogdanite low-pressure transition. *American Mineralogist*, **108**, 1506–1515.

Galuskina I.O., Galuskin E.V. and Vapnik Y.A. (2016) Terrestrial merrillite. *Plinius*, **42**, 563 [2nd European Mineralogical Conference. Abstract].

Galuskina I.O., Galuskin E.V., Pakhomova A.S., Widmer R., Armbruster T., Krüger B., Grew E.S., Vapnik Y., Dzierażanowski P. and Murashko M. (2017a) Khesinite, $Ca_4Mg_2Fe^{3+}_{10}O_4$ [$(Fe^{3+}_{10}Si_2)O_{36}$], a new rhönite-group (sapphirine supergroup) mineral from the Negev Desert, Israel—Natural analogue of the SFCA phase. *European Journal of Mineralogy*, **29**, 101–116.

Galuskina I.O., Galuskin E.V., Prusik K., Vapnik Y., Juroszek R., Jeżak L. and Murashko M. (2017b) Dzierżanowskite, $CaCu_2S_2$ – a new natural thiocuprate from Jabel Harmun, Judean Desert, Palestine Autonomy, Israel. *Mineralogical Magazine*, **81**, 1073–1085.

Galuskina I.O., Galuskin E.V., Vapnik Y., Prusik K., Stasiak M., Dzierżanowski P. and Murashko M. (2017c) Gurimite, $Ba_3(VO_4)_2$ and hexacelsian, $BaAl_2Si_2O_8$ - Two new minerals from schorlomite-rich paralava of the Hatrurim Complex, Negev Desert, Israel. *Mineralogical Magazine*, 81, 1009–1019.

Geller Y.I., Burg A., Halicz L. and Kolodny Y. (2012) System closure during the combustion metamorphic Mottled Zone event, Israel. *Chemical Geology*, **334**, 25–36.

Gross S. (1977) The mineralogy of the Hatrurim Formation, Israel. *Geological Survey* of *Israel Bulletin*, **70**, 1–80.

Gross S. (1984) Occurrence of ye'elimite and ellestadite in an unusual cobble from the „pseudo-conglomerate" of the Hatrurim Basin. *Geological Survey* of *Israel Bulletin*, **84**, 1–4.

Hughes J.M., Jolliff B.L. and Rakovan J. (2008) The crystal chemistry of whitlockite and merrillite and the dehydrogenation of whitlockite to merrillite. *American Mineralogist*, **93**, 1300–1305.

Hwang S.L., Shen P., Chu H.T., Yui T.F., Varela M.E. and Iizuka Y. (2019) New minerals tsangpoite $Ca_5(PO_4)_2(SiO_4)$ and matyhite $Ca_9(Ca_{0.5}\square_{0.5})Fe(PO_4)_7$ from the D'Orbigny angrite. *Mineralogical Magazine*, **83**, 293–313.

Jolliff B.L., Hughes J.M., Freeman J.J. and Zeigler R.A. (2006) Crystal chemistry of lunar merrillite and comparison to other meteoritic and planetary suites of whitlockite and merrillite. *American Mineralogist*, **91**, 1583–1595.

Khoury H.N., Sokol E.V., Kokh S.N., Seryotkin Y.V., Nigmatulina E.N., Goryainov S.V., Belogub E.V. and Clark I.D. (2016) Tululite, $Ca_{14}(Fe^{3+}, Al)(Al,Zn,Fe^{3+},Si,P,Mn, Mg)_{15}O_{36}$: a new Ca zincate-aluminate from combustion metamorphic marbles, Central Jordan. *Mineralogy and Petrology*, **110**, 125–140.

Kolodny Y. and Gross S. (1974) Thermal metamorphism by combustion of organic matter: isotopic and petrological evidence. *Journal of* Geology, **82**, 489–506.

Krüger B., Galuskin E.V., Galuskina I.O., Krüger H. and Vapnik Ye. (2021) Kahlenbergite $KAl_{11}O_{17}$, a new – alumina mineral and Fe-rich hibonite from the Hatrurim Basin, the Negev desert, Israel. *European Journal of Mineralogy*, **33**, 341–355.

Krzątała A., Krüger B., Galuskina I., Vapnik Y. and Galuskin E. (2020) Walstromite, $BaCa_2(Si_3O_9)$, from Rankinite Paralava within Gehlenite Hornfels of the Hatrurim Basin, Negev Desert, Israel. *Minerals*, **10**, 407.

Lazoryak B.I., Morozov V.A., Belik A.A., Khasanov S.S. and Shekhtman V.Ch. (1996) Crystal structures and characterization of $Ca_9Fe(PO_4)_7$ and $Ca_9FeH_{0.9}(PO_4)_7$. *Journal of Solid State Chemistry*, **122**, 15–21.

Lazoryak B.I., Deyneko D.V., Aksenov S.M., Stefanovich S.Yu., Fortalnova E.A., Petrova D.A., Baryshnikova O.V., Kosmyna M.B. and Shekhovtsov A.N. (2018) Pure, lithium- or magnesium-doped ferroelectric single crystals of $Ca_9Y(VO_4)_7$: cation arrangements and phase transitions. *Zeitschrift für Kristallographie*, **233**, 1–11.

Li T., Li Z., Huang Z., Zhong J., Fan G., Guo D., Qin M., Zhang J., Li J., Liu H., Qiu L., Wang F., He S., Yu A., Liu R., Wu Y., Deng L., Tai Z., He Y. and Lin Y. (2022) Changesite-(Y), IMA 2022–023. CNMNC Newsletter 69; *Mineralogical Magazine*, **86**, 988–992.

Matthews A. and Gross S. (1980) Petrologic evolution of the Mottled Zone (Hatrurim) metamorphic complex of Israel. *Israel Journal* of *Earth Sciences*, **29**, 93–106.

Murashko M.N., Britvin S.N., Vapnik Ye., Polekhovsky Y.S., Shilovskikh V.V., Zaitsev A.N. and Vereshchagin O.S. (2022) Nickolayite, FeMoP, a new natural molybdenum phosphide. *Mineralogical Magazine*, **86**, 749–757.

Novikov I., Vapnik Ye. and Safonova I (2013) Mud volcano origin of the Mottled Zone, South Levant. *Geoscience* Frontiers, **4**, 597–619.

Rigaku Oxford Diffraction (2019) *CrysAlis PRO*. Rigaku Oxford Diffraction, Yarnton, England.

Schmieder M., Buchner E. and Kröchert J. (2009) "Ballen silica" in impactites and magmatic rocks. *Abstracts* 40*th Lunar and Planetary Science Conference*. Texas, USA.

Shahar Y., Yaacov N. and Yair S (1989) Two close associations: Si-P-Fe and Si-P-C in the Upper Campanian and Lower Maastrichtian sediments of the Negev, Israel. *Sciences Géologiques, bulletins et mémoires*, **42**, 155–171.

Sheldrick G.M. (2015a) SHELXT – Integrated space-group and crystal-structure determination. *Acta Crystallographica*, **A71**, 3–8.

Sheldrick G.M. (2015b) Crystal structure refinement with SHELXL. *Acta Crystallographica*, **C71**, 3–8.

Sokol E., Novikov I., Zateeva S., Vapnik Ye., Shagam R. and Kozmenko O. (2010) Combustion metamorphism in the Nabi Musa dome: New implications for a mud volcanic origin of the Mottled Zone, Dead Sea area. *Basin Research*, **22**, 414–438.

Solecka U., Bajda T., Topolska J., Zelek-Pogudz S. and Manecki M. (2018) Raman and Fourier transform infrared spectroscopic study of pyromorphite-vanadinite solid solutions. *Spectrochimica Acta, Part A: Molecular and Biomolecular Spectroscopy*, **190**, 96–103.

Sugiyama K. and Tokonami M. (1987) Structure and crystal chemistry of a dense polymorph of tricalcium phosphate $Ca_3(PO_4)_2$: a host to accommodate large lithophile elements in the Earth's mantle. *Physics and Chemistry of Minerals*, **15**, 125–130

Vapnik Y., Sharygin V.V., Sokol E.V. and Shagam R. (2007) Paralavas in a combustion metamorphic complex: Hatrurim Basin, Israel. *Reviews in Engineering Geology*, **18**, 1–21.

Ward D., Bischoff A., Roszjar J., Berndt J. and Whitehouse M.J. (2017) Trace element inventory of meteoritic Ca-phosphates. *American Mineralogist*, **102**, 1856–1880.

Wherry E.T. (1917) Merrillite, meteoritic calcium phosphate. *American Mineralogist*, **2**, 119–119.

Witzke T., Phillips B.L., Woerner W., Countinho J.M.V., Färber G. and Contreira Filho R.R. (2015) Hedegaardite, IMA 2014-069. CNMNC Newsletter No. 23, February 2015, page 54. *Mineralogical Magazine*, **79**, 51–58.

Xie X., Minitti M.E., Chen M., Mao H.-K., Wang D., Shu J. and Fei Y. (2003) Tuite, γ-$Ca_3(PO_4)_2$ – A new mineral from the Suizhou L6 chondrite. *European Journal of Mineralogy*, **15**, 1001–1005.

Xie X., Yang H., Gu X., Downs R.T. (2015) Chemical composition and crystal structure of merrillite from the Suizhou meteorite. *American Mineralogist*, **100**, 2753–2756.

https://doi.org/10.1180/mgm.2023.71 Published online by Cambridge University Press